analytical chemistry

pubs.acs.org/ac Article

Signal "On-Amplified-Off" Strategy Based on Hafnium Dioxide Nanomaterials as Electrochemiluminescence Emitters for Progesterone Detection

Xue Dong, Qingze Zeng, Li Dai, Xiang Ren, Wei Cao, Huangxian Ju,* and Qin Wei*

Cite This: *Anal. Chem.* 2023, 95, 12184−12191 Read Online

ACCESS | Metrics & More | Article Recommendations | Supporting Information

ABSTRACT: When consumed, excess progesterone (P4)—found in food and the environment—can lead to severe illnesses in humans. Therefore, quantitative analysis of P4 is critical for identifying its hazardous levels. In this study, a novel signal "on-amplified-off" P4 detection mode was proposed, which was based on the utilization of hafnium oxide (HfO_2) as a unique electrochemiluminescence (ECL) emitter, produced by calcining UiO-66(Hf). This is the first time that HfO_2 has been used as an ECL emitter. HfO_2 displayed excellent conductivity and a high specific surface area, allowing it to connect with numerous aptamers and produce a "signal-on" effect. Ni-doped ZnO (Ni-ZnO) acted as a coreaction accelerator, enhancing the ECL strength of HfO_2 by generating more tripropylamine radicals. cDNA was labeled with Ni-ZnO, and Ni-ZnO was linked to the aptamer via base complementary pairing, affording "signal-amplified". The presence of the target molecule P4 instigated a specific binding process with the aptamer, triggering the shedding of cDNA-Ni-ZnO and resulting in "signal-off". This novel "on-amplified-off" strategy effectively improved the sensitivity and specificity of P4 analysis, introducing a practical method for detecting biomolecules beyond the scope of this study, which holds immense potential for future applications.

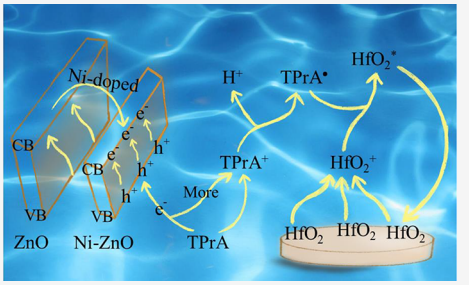

INTRODUCTION

Progesterone (P4) is a bioactive hormone secreted by the ovary, but it is also found in the environment and food.[1−3] P4 can be present in wastewater, surface water, and food products such as meat, milk, and eggs owing to the use of P4-based veterinary drugs in animal husbandry and the excretion of P4 by humans and animals. High concentrations of P4 in the environment may exert detrimental effects on fish and amphibians and promote algal growth and eutrophication in water bodies, disturbing the biodiversity and ecological stability of aquatic ecosystems. Consuming P4-rich food may disrupt the production, transportation, and metabolism of normal endocrine substances in the human body.[4,5] Hence, accurate detection of P4 levels in environmental and food samples with high sensitivity is crucial.

Aptamers are short oligonucleotide sequences that are screened in vitro to specifically bind to target molecules such as proteins or small molecules.[6,7] They offer advantages over antibodies, including simple chemical synthesis or modification, high stability, easy storage, and a wide range of target recognition.[8,9] Their high affinity and selectivity render them ideal for numerous applications, including cell imaging, disease treatment, and biosensor analysis.[10−15] An electrochemiluminescence (ECL) aptasensor, created by combining an aptamer as a recognition module with the ECL technology, offers superior sensitivity, low background signal, simple operation, and rapid analysis.[16,17] An ECL aptasensor typically immobilizes the aptamer onto an electrode surface and employs a luminescent molecule to label it. The emergence of the ECL aptasensor has immensely enhanced the sensitivity and specificity of analyzing small molecular targets such as toxins, antibiotics, and hormones.[18−21]

Recently, hafnium (Hf)—which belongs to the same group as titanium and zirconium—has been receiving increasing attention. Hafnium dioxide (HfO_2), the primary oxide of Hf, is commonly used in optical coatings, refractory materials, and catalysts.[22−25] At a nanoscale, HfO_2 displays improved properties, such as an enlarged surface area and increased catalytic activity.[26−28] In this study, a fluorine-containing organic ligand, tetrafluoroterephthalic acid, was used to synthesize the metal−organic framework (MOF) material UiO-66(Hf). This material was subsequently calcined to obtain HfO_2. The resultant HfO_2 exhibited a large specific surface area and satisfactory conductivity, crystallinity, and stability. This is the first study to investigate and report the ECL properties of HfO_2, offering new application prospects for the development of HfO_2.

Received: July 1, 2023
Accepted: July 23, 2023
Published: August 2, 2023

https://doi.org/10.1021/acs.analchem.3c02861
Anal. Chem. 2023, 95, 12184−12191

The ECL binary system of "luminophore/coreagent" typically comprises an ECL emitter and a coreagent with high electrochemical redox activity, enhancing the luminescence intensity and stability of the luminophore.[29−31] The ECL ternary system includes a coreaction accelerator that interacts with the coreagent to increase the generation of intermediates, thus boosting the luminescence intensity of the luminophore through the interaction between the intermediates.[32−35] The "coreaction accelerator" concept marks a major step toward constructing a novel and efficient ECL ternary system.

In this study, HfO_2 was used as the substrate material and the aptamer was connected to this substrate via the Hf−O−P bonds formed between Hf and phosphate groups.[36,37] HfO_2 served as the luminophore for generating the initial luminescence signal ("signal-on"). cDNA was labeled with Ni-doped ZnO (Ni-ZnO) nanomaterials that were used as coreaction accelerators. The ECL signal of HfO_2 was effectively enhanced after the complementary base pairing of cDNA with the aptamer ("signal-amplified"). However, the introduction of target P4 caused the detachment of cDNA from the electrode, resulting in a reduced luminescence signal ("signal-off"). The aptasensor built based on the signal "on-amplified-off" strategy can sensitively detect the P4 content.

EXPERIMENTAL SECTION

Detailed descriptions of the reagents and materials, apparatus, and ECL measurement parameters of P4 are displayed in the Supporting Information.

Preparation of HfO_2 and HfO_2-Aptamer. HfO_2 was obtained by calcining the MOF material UiO-66(Hf). First, UiO-66(Hf) was synthesized on the basis of literature reports:[38] 5 mmol of tetrafluoroterephthalic acid and 5 mmol of $HfCl_4$ were dissolved in a solution of water (30 mL) and acetic acid (20 mL). The resultant mixture was stirred at 100 °C for 24 h, followed by centrifugation, washing, and drying to obtain UiO-66(Hf) powder. UiO-66(Hf) was calcined at 700 °C for 4 h in a muffle furnace with a heating rate of 2.5 °C/min to obtain HfO_2. Aptamer solution (1 mL) (10 μmol/L) was mixed with HfO_2 and shaken for 12 h. The resulting mixture was subsequently centrifuged once to obtain HfO_2-aptamer.

Preparation of Ni-ZnO and cDNA-Ni-ZnO. The ZnNi-MOF was synthesized using a method described in previous literature.[39] $Zn(NO_3)_2{\cdot}6H_2O$ (490 mg), $Ni(NO_3)_2{\cdot}6H_2O$ (95 mg), and 2-methylimidazole (1.23 g) were thoroughly dissolved in 60 mL of ethanol and stirred at room temperature for 24 h. Subsequently, the mixture was centrifuged at 13,000 rpm and washed twice with methanol. After drying and grinding, the resulting light violet precipitate was identified as ZnNi-MOF. ZnNi-MOF was calcined at 400 °C for 3 h in a muffle furnace with a heating rate of 2 °C/min to obtain Ni-ZnO nanomaterials. cDNA solution (1 mL) (10 μmol/L) was mixed with Ni-ZnO and shaken for 12 h. Subsequently, the mixture was centrifuged once to obtain cDNA-Ni-ZnO.

Fabrication of the ECL Aptasensor. To prepare the aptasensor, it was necessary to begin by polishing the bare glass carbon electrode (GCE) with polishing powder until a mirror surface was achieved. Prior to oxidation of the bare electrode, 8 μL of HfO_2-aptamer was added to the electrode surface and left to dry for approximately 1 h. Next, 3 μL of BSA (1%) was dripped on the electrode and rinsed with PBS once the electrode had dried. Whereafter, 8 μL of cDNA-Ni-ZnO was dispersed on the modified electrode and allowed to dry for approximately 1 h. The modified electrode can then be immersed in different concentrations of P4 solution to enable full binding of the aptamer to the target. The prepared aptasensor was ready for subsequent testing (Scheme 1).

Scheme 1. Fabrication Scheme of the ECL Aptasensor

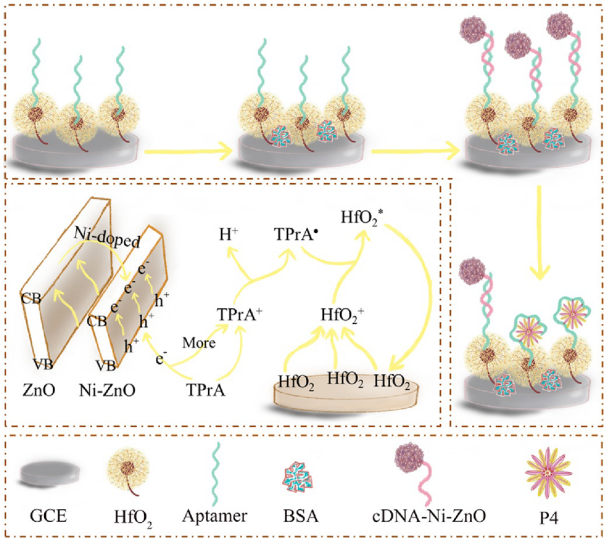

RESULTS AND DISCUSSION

Characterization of HfO_2 and Ni-ZnO. The synthesized nanomaterials were characterized using SEM, TEM, XPS, and XRD techniques. The SEM images revealed that UiO-66(Hf) exhibited a large flower-shaped structure (Figure 1A), while

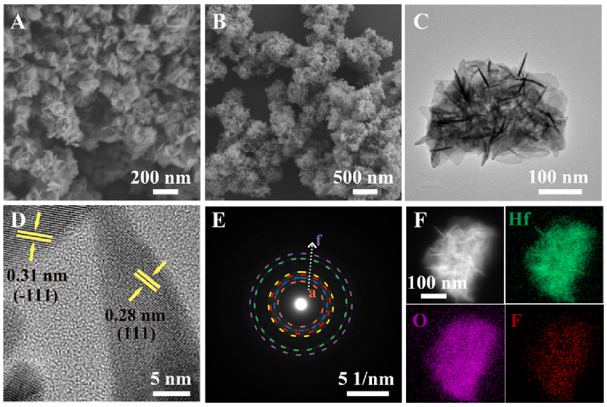

Figure 1. SEM images of (A) UiO-66(Hf) and (B) HfO_2; (C) TEM, (D) HRTEM, (E) TEM diffraction, and (F) mapping of HfO_2.

HfO_2 obtained after calcination assembled from thinner nanosheets with a size range of 300−500 nm (Figure 1B). The mapping diagram of HfO_2 nanomaterials showed that the three elements Hf, O, and F are evenly distributed (Figure 1F). The XRD spectra of Figure 2A confirmed that UiO-66(Hf) had good crystallinity and was consistent with literature reports,[38] while XRD of HfO_2 indicated the synthesis of the monoclinic structure (JCPDS card 34-0104). Furthermore, the lattice spacing of 0.31 and 0.28 nm in Figure 1D corresponded to the (−111) and (111) crystal planes of HfO_2, respectively. The crystal planes of HfO_2 were further analyzed by diffraction. Figure 1E shows that the diffraction rings of a−f

https://doi.org/10.1021/acs.analchem.3c02861
Anal. Chem. 2023, 95, 12184−12191

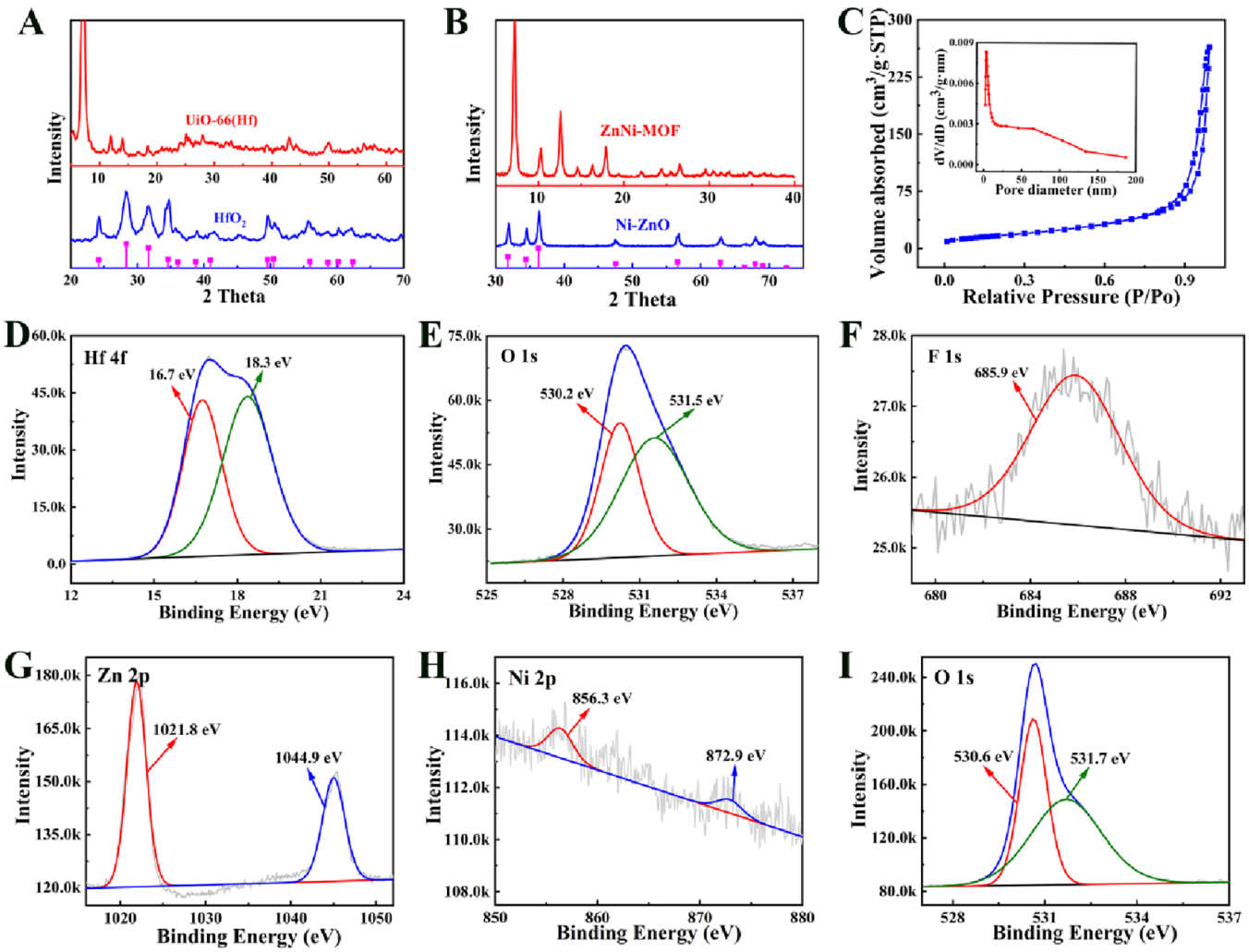

Figure 2. XRD of (A) UiO-66(Hf) and HfO_2 and (B) ZnNi-MOF and Ni-ZnO; (C) N_2 adsorption−desorption isotherm and pore size distribution (illustration) of HfO_2; XPS spectra of HfO_2 and Ni-ZnO: (D) Hf 4f, (E) O 1s, (F) F 1s, (G) Zn 2p, (H) Ni 2p, and (I) O 1s.

corresponded to the (011), (−111), (111), (200), (022), and (−311) crystal planes of HfO_2. The N_2 adsorption−desorption isotherm of HfO_2 is shown in Figure 2C. The BET specific surface area of the synthesized HfO_2 was 61.63 m^2/g, and the average pore size was 26.59 nm (illustration of Figure 2C). Meanwhile, Figure 2D exhibits two separate peaks at 16.7 and 18.3 eV in the XPS spectra, which were attributed to the Hf $4f_{7/2}$ and $4f_{5/2}$ orbitals, respectively. The two peaks at 530.2 and 531.5 eV in Figure 2E represented the lattice oxygen of HfO_2 and surface oxygen, respectively. The peak at 685.9 eV in Figure 2F corresponded to the F 1s orbital.

The morphology, crystal form, and structure of the synthesized ZnNi-MOF and Ni-ZnO were analyzed. ZnNi-MOF was found to be a bulk nanomaterial with an approximate diameter of 50 nm (Figure 3A), while the size of Ni-ZnO decreased to around 35 nm after calcination (Figure 3B). Figure 3E reveals a uniform distribution of Zn, Ni, and O throughout the materials based on the mapping characterization. The crystal structure of both materials is tested in Figure 2B, and the XRD results confirmed that the crystal structure of ZnNi-MOF was consistent with literature.[39] The Ni-doped ZnO showed no distinct change compared to undoped ZnO, indicating a zincite structure (JCPDS card 36-1451), which was likely due to the low level of Ni doping. The

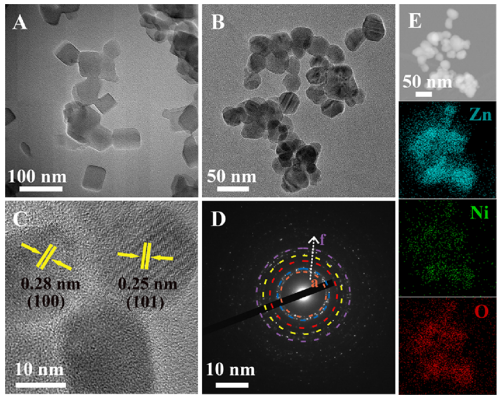

Figure 3. TEM images of (A) ZnNi-MOF and (B) Ni-ZnO; (C) HRTEM, (D) TEM diffraction, and (E) mapping of Ni-ZnO.

HRTEM revealed a corresponding relationship between lattice spacing of 0.28 and 0.25 nm and crystal planes (101) and (100), respectively (Figure 3C). Moreover, the existence of the crystal planes (100), (101), (102), (110), (103), and (112) was confirmed by measuring the diffraction rings a−f (Figure 3D). The utilization of the XPS spectrum on Ni-ZnO facilitated the determination of surface elemental composition

https://doi.org/10.1021/acs.analchem.3c02861
Anal. Chem. 2023, 95, 12184−12191

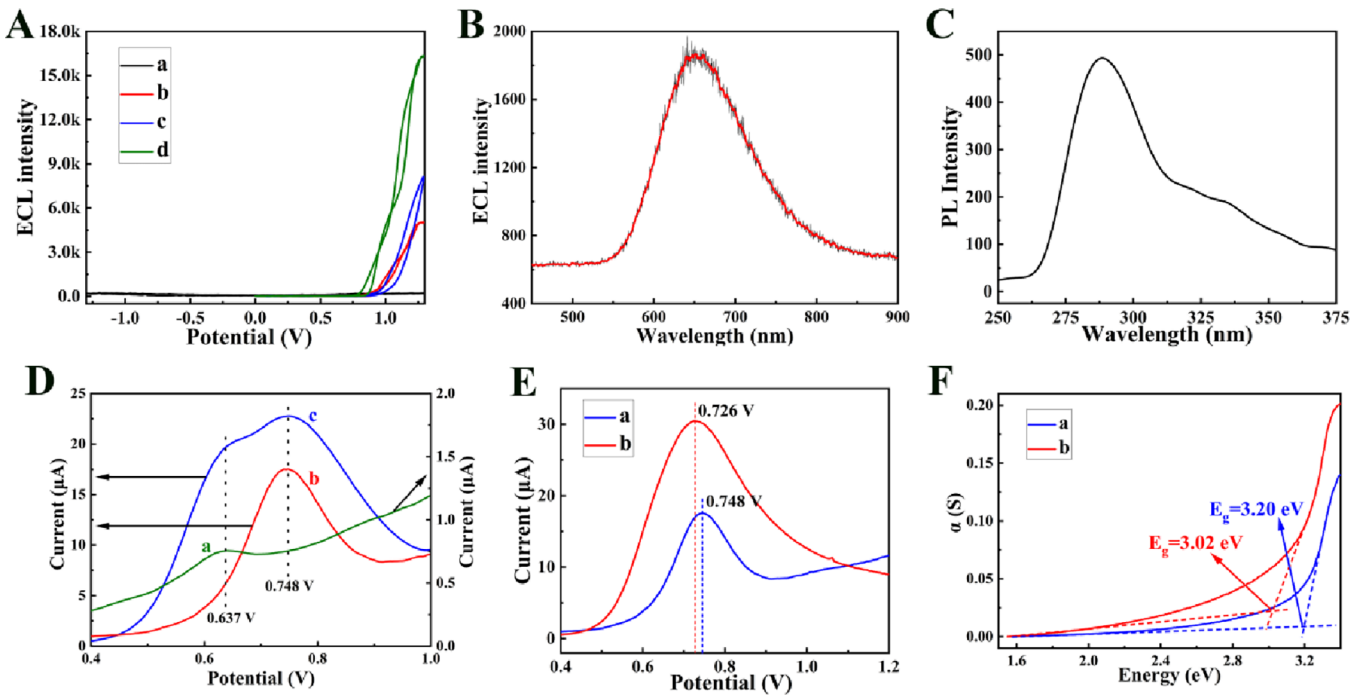

Figure 4. (A) ECL intensity of GCE/HfO_2 in PBS (a) and PBS containing 15 mmol/L TPrA (b), GCE/HfO_2/ZnO (c), and GCE/HfO_2/Ni-ZnO (d) in PBS containing 15 mmol/L TPrA; (B) ECL emission spectrum and (C) PL spectrum of HfO_2; (D) DPV curves of GCE/HfO_2 in PBS (a), bare GCE (b), and GCE/HfO_2 (c) in PBS containing 15 mmol/L TPrA; (E) DPV curves of bare GCE (a) and GCE/Ni-ZnO (b) in PBS containing 15 mmol/L TPrA; (F) UV−vis diffuse-reflectance spectra of ZnO (a) and Ni-ZnO (b).

as well as the chemical structure.[40] In Figure 2G, the presence of Zn^{2+} was confirmed by the two peaks at 1021.8 and 1044.9 eV corresponding to Zn $2p_{3/2}$ and Zn $2p_{1/2}$ respectively. Meanwhile, Figure 2H shows that the peaks observed at 856.3 and 872.9 eV represented the Ni $2p_{3/2}$ and Ni $2p_{1/2}$ orbits, respectively. In Figure 2I, the lattice oxygen of Ni-ZnO and the surface oxygen were distinguished by the peaks observed at 530.6 and 531.7 eV, respectively.

Mechanism Investigation of ECL and Amplification. The main signal output of the constructed aptasensor comes from the HfO_2 luminophore. Therefore, the luminescence mechanism of HfO_2 had been studied and discussed. The luminescence of ECL emitters typically involves two pathways: annihilation type and coreactant participation type.[41,42] To investigate the luminescence type, HfO_2 modified electrodes were preliminarily tested in both PBS and PBS containing coreactant. At a potential range of −1.3 to 1.3 V, the orderly ECL emission of HfO_2 using PBS as the electrolyte had not been observed, indicating that the ECL emission of HfO_2 was not carried out through an annihilation pathway (Figure 4A, curve a). Subsequently, the potential was adjusted to 0−1.3 V, and an ECL test was conducted on the modified electrode with tripropylamine (TPrA) as a coreactant. The experimental results demonstrated a noteworthy enhancement in the ECL emission of HfO_2 (Figure 4A, curve b). The ECL emission spectrum (Figure 4B) and photoluminescence (PL) spectrum (Figure 4C) of HfO_2 were measured, and the PL spectrum exhibited a redshift of 360 nm in comparison to the ECL emission position situated at 650 nm. This observation suggested the surface state emission of HfO_2.[43] The oxidation state of the HfO_2 modified electrode in different solutions was investigated. As shown in Figure 4D, the electrochemical properties of HfO_2 were evaluated by performing differential pulse voltammetry (DPV) in PBS with and without TPrA. Under a scanning voltage of 0−1.3 V, HfO_2 exhibited a peak potential of 0.637 V in PBS without TPrA (curve a). The bare electrode showed an oxidation peak at 0.748 V in PBS containing TPrA (curve b). When the GCE/HfO_2 was tested in PBS containing TPrA, two peaks corresponding to the oxidation of HfO_2 and TPrA were observed (curve c), along with an obvious increase in the oxidation current. The experimental results provided positive evidence supporting the ECL mechanism of HfO_2. Drawing upon experimental observations and prior research, the ECL mechanism of HfO_2 had been postulated.[44,45] Specifically, when a positive potential was applied to the electrode, the loss of electrons from TPrA and HfO_2 yielded $TPrA^+$ and HfO_2^+, respectively (eqs a and b). The former was subsequently deprotonated to engender TPrA free radicals, denoted as $TPrA^\bullet$ (eq c). The interaction between $TPrA^\bullet$ and HfO_2^+ culminated in the production of excited state HfO_2* (eq d), with ECL emission being realized during the ensuing transition of HfO_2 from its excited state back to the ground state (eq d).

$$TPrA - e \rightarrow TPrA^+ \quad (a)$$

$$HfO_2 - e \rightarrow HfO_2^+ \quad (b)$$

$$TPrA^+ - H^+ \rightarrow TPrA^\cdot \quad (c)$$

$$HfO_2^+ + TPrA^\cdot \rightarrow HfO_2^* \quad (d)$$

$$HfO_2^* \rightarrow HfO_2 + h\nu \quad (e)$$

The aptasensor was equipped with a signal amplification mechanism to ensure or enhance its sensitivity, thus requiring a thorough investigation into the ECL amplification mechanism. The ECL signals were tested for GCE/HfO_2, GCE/HfO_2/ZnO, and GCE/HfO_2/Ni-ZnO modified electrodes. Figure 4A shows that the ECL signal of HfO_2 was amplified from 5000

https://doi.org/10.1021/acs.analchem.3c02861
Anal. Chem. 2023, 95, 12184−12191

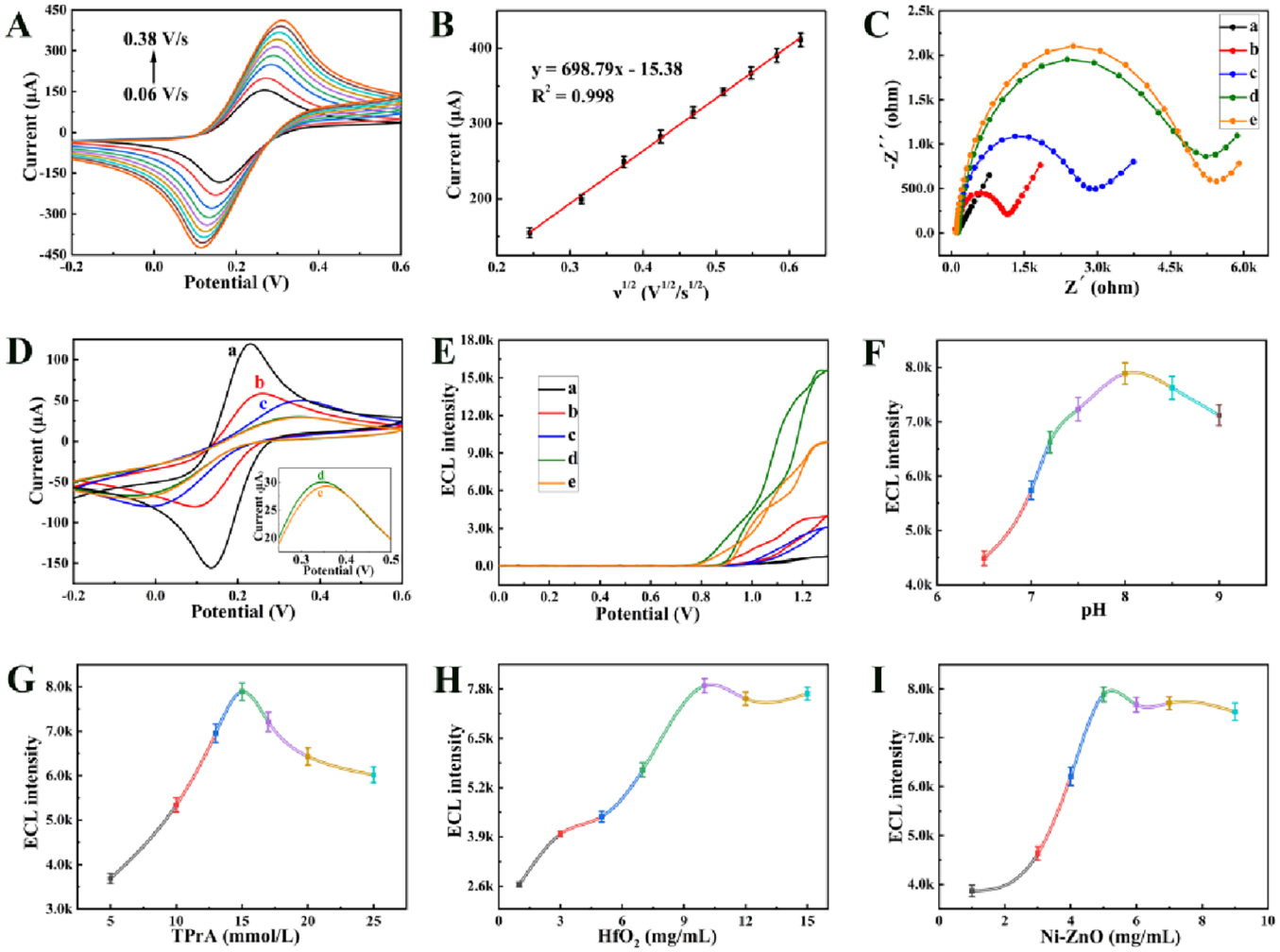

Figure 5. (A) CV curves of HfO_2 with the scanning rates from 60 to 380 mV/s; (B) calibration curve of reduction peak current I_p and the square root of scanning rate $v^{1/2}$; (C) EIS, (D) CV, and (E) ECL intensity of bare GCE (a), GCE/HfO_2-aptamer (b), GCE/HfO_2-aptamer/BSA (c), GCE/HfO_2-aptamer/BSA/DNA-Ni-ZnO (d), and GCE/HfO_2-aptamer/BSA/DNA-Ni-ZnO/P4 (e); optimization of (F) pH and the concentration of (G) TPrA, (H) HfO_2, and (I) Ni-ZnO.

a.u. (curve b) to approximately 8000 a.u. (curve c) by undoped ZnO, while the Ni-ZnO modified electrode yielded an ECL intensity increase up to about 16,000 a.u. (curve d). The oxidation potential of TPrA was measured using DPV (Figure 4E). The bare electrode displayed an oxidation peak at approximately 0.5 V with a maximum value of 0.748 V. After modification with Ni-ZnO, the oxidation potential of TPrA was reduced by 0.022 V and the current value notably increased. Therefore, it was speculated that Ni-ZnO can facilitate the oxidation of TPrA, thereby increasing the ease of oxidation and production of TPrA free radicals.[46] Furthermore, the bandgap energy (E_g) of ZnO and Ni-ZnO was determined and calculated (Figure 4F). Notably, when contrasted with ZnO, the E_g of Ni-ZnO was narrowed by 0.18 eV, thus implying that Ni-ZnO was more susceptible to electronic transitions. Once the internal electrons in Ni-ZnO transitioned from the valence band to the conduction band, the electrons produced in the TPrA oxidation reaction reacted with the holes, thereby facilitating the oxidation reaction of TPrA and promoting the production of a greater abundance of free radicals.[47]

ECL Efficiency of the Luminophore. The ECL efficiency of the luminophore was evaluated employing $[Ru(bpy)_3]^{2+}$ as the benchmark according to the reported method.[46] Subsequently, the relative Φ_{ECL} was determined utilizing the following formula:

$$\Phi_{ECL} = \Phi^0{}_{ECL}(IQ^0{}_f/Q_fI^0)$$

The aforementioned $\Phi^0{}_{ECL}$ corresponded to the ECL annihilation efficiency of 1 mmol/L $[Ru(bpy)_3]^{2+}$ in 0.1 mol/L $TBAPF_6$/acetonitrile and yields a value of 5.0%. The parameter Φ_{ECL} value was determined by examining the luminophore in PBS containing 15 mmol/L TPrA (pH = 8.0) at a potential of 0−1.3 V. I and Q_f indicated the ECL intensity and corresponding Faraday charges of the luminophore, respectively, whereas I^0 and Q^0_f stood for the ECL intensity and corresponding Faraday charges of $[Ru(bpy)_3]^{2+}$. Based on the above methodology, the calculated ECL efficiencies for HfO_2 and HfO_2/Ni-ZnO were 1.1 and 4.6%, respectively, demonstrating that the loading of Ni-ZnO effectively heightened the ECL efficiency of the luminophore.

Characterization and Optimization on the Aptasensor Construction Process. The electrochemically active area of the substrate material served as a critical indicator in the construction of the aptasensor. The cyclic voltammetry (CV) of HfO_2 was conducted at different scanning rates ranging from 0.06 to 0.38 V/s (Figure 5A,B). Analysis and calculations

https://doi.org/10.1021/acs.analchem.3c02861
Anal. Chem. 2023, 95, 12184−12191

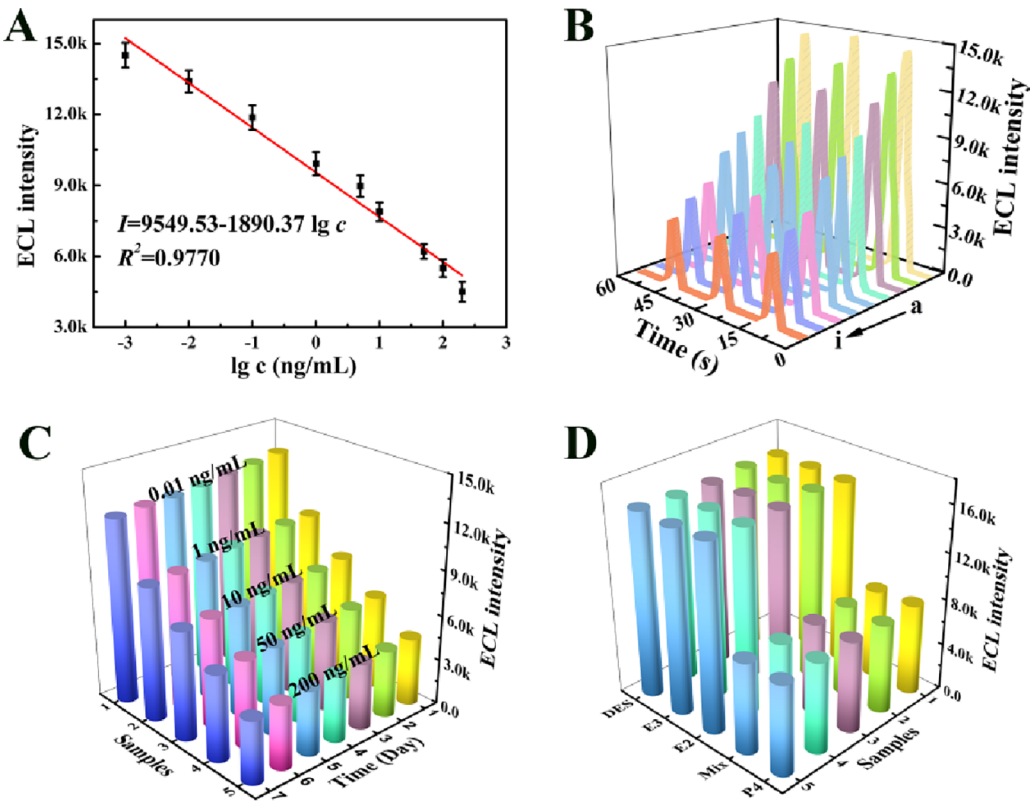

Figure 6. (A) Linear relationship between the logarithm of P4 concentration and ECL intensity; (B) ECL intensity for a range of P4 concentrations (0.001, 0.01, 0.1, 1, 5, 10, 50, 100, and 200 ng/mL); (C) 7 days' stability of the aptasensor with different P4 concentrations; (D) specificity of the aptasensor.

of the results revealed that the electrochemically active area of HfO_2 reached 0.4012 cm^2, which was observably greater than the 0.1256 cm^2 of the bare electrode (Φ = 4 mm). This observation underscored the ability of HfO_2 to enhance aptasensor sensitivity via its increased capacity to accommodate more aptamers.

To ensure the successful assembly of the aptasensor, a combination of electrochemical impedance spectroscopy (EIS) (Figure 5C), CV (Figure 5D), and ECL (Figure 5E) tests were employed. The bare electrode exhibited excellent conductivity, which resulted in low impedance and high current (curve a). However, due to the absence of the luminophore, the ECL signal was negligible (curve a). Upon modification of the electrode with HfO_2-aptamer, the resistance increased while the current decreased (curve b). Meanwhile, the ECL signal of approximately 4000 a.u. was observed (curve b). The addition of BSA resulted in a reduced conductivity and ECL signal (curve c). Subsequent modification of the electrode with cDNA-Ni-ZnO further attenuated the conductivity (curve d). However, the Ni-ZnO as a coreaction accelerator observably amplified ECL emission of HfO_2 (curve d). Finally, the addition of target P4 triggered the detachment of some cDNA-Ni-ZnO from the electrode, leading to a slight change in the conductivity and a notable decrease in the ECL signal (curve e). Taken together, these experimental findings serve as strong evidence to confirm the successful construction of the aptasensor.

To achieve the optimal detection performance of the aptasensor for P4, various experimental parameters, including the pH (Figure 5F) of PBS and the concentration of TPrA (Figure 5G), HfO_2 (Figure 5H), and Ni-ZnO (Figure 5I), were optimized through multiple parallel tests. Ultimately, the aptasensor was constructed using 10 mg/mL HfO_2 and 5 mg/mL Ni-ZnO, with the detection solution consisting of PBS containing 15 mmol/L TPrA at pH 8.0.

Performance of the ECL Aptasensor. The performance of the aptasensor in detecting P4 is of crucial importance. As depicted in Figure 6B, the aptasensor response was evaluated for a range of P4 concentrations. The results indicated that the aptasensor assembled using varying concentrations of P4 (0.001−200 ng/mL) demonstrated remarkable stability following multiple scans. Furthermore, the elevation in the P4 concentration led to an increased detachment of DNA-Ni-ZnO from the electrode, thereby causing a gradual decline in the signal value of the aptasensor. Based on calculations and fitting, the linear correlation was observed between the logarithm of P4 concentration and ECL intensity, as evidenced by the linear equation I = 9549.53−1890.3 lg c (R^2 = 0.9770) (Figure 6A). The aptasensor demonstrated a remarkable sensitivity with a minimum detection limit of 0.39 pg/mL. To thoroughly assess the analytical capacity of the developed aptasensor for P4, a comparative analysis was conducted with previously reported methods. The results illustrated in Table S1 demonstrated that our method exhibited a broad linear range and a lower detection limit, highlighting its exceptional performance for P4 analysis. Additionally, the aptasensors fabricated with five distinct concentrations of P4 displayed excellent stability within a period of 7 days (Figure 6C). To assess the specificity of the aptasensor in detecting target P4 (10 ng/mL), DES (100 ng/mL), E3 (100 ng/mL), and E2 (100 ng/mL) were employed as interference factors. Five identical electrodes were utilized for detecting diverse target

https://doi.org/10.1021/acs.analchem.3c02861
Anal. Chem. 2023, 95, 12184−12191

substances, and the outcomes confirmed the superior specificity and repeatability of the aptasensor (Figure 6D).

Sample Analysis. The detection capability of P4 in both environmental and food samples holds equal importance for the aptasensor. In this study, spiked recovery methodology was utilized to evaluate the analytical performance of the samples. Pre-treatment was not necessary for tap water. For milk samples, 5 mL of milk was diluted with 90 mL of PBS and 5 mL of 18 mmol/L $CaCl_2$ was added for thorough blending. The supernatant of the mixture after centrifugation (6000 rpm, 10 min) was collected. P4 standard solutions with varying concentrations were added to both tap water and milk samples. As indicated in Table S2, no content of P4 was detected in the samples without the addition of P4 standard solutions. The sample recovery rates for standard solutions with concentrations of 10 pg/mL, 1 ng/mL, and 5 ng/mL P4 were found to be between 97.0 and 103%, with an RSD between 2.4 and 4.9%, which demonstrated the high potential of the aptasensor for detecting P4 in environmental and food samples.

CONCLUSIONS

Herein, HfO_2 was developed as a novel ECL emitter for the first time, with a comprehensive investigation of its morphology, performance, and luminescence mechanism. A novel aptasensor construction strategy based on the ECL emitter HfO_2 was presented, referred to as signal "on-amplified-off". HfO_2 was used as a luminophore for the "signal-on" phenomenon, and Ni-ZnO served as the coreaction accelerator for the "signal-amplified" response. The introduction of the target molecule P4 caused the detachment of Ni-ZnO, resulting in a "signal-off" response. This newly developed sensing strategy demonstrated high sensitivity and specificity in detecting P4, indicating promising potential for its application in environmental and food samples.

ASSOCIATED CONTENT

Supporting Information

The Supporting Information is available free of charge at https://pubs.acs.org/doi/10.1021/acs.analchem.3c02861.

Reagents and materials; apparatus; ECL measurement parameters of P4; necessary supporting tables (PDF)

AUTHOR INFORMATION

Corresponding Authors

Huangxian Ju − *Key Laboratory of Interfacial Reaction & Sensing Analysis in Universities of Shandong, Collaborative Innovation Center for Green Chemical Manufacturing and Accurate Detection, School of Chemistry and Chemical Engineering, University of Jinan, Jinan 250022, P. R. China; State Key Laboratory of Analytical Chemistry for Life Science, School of Chemistry and Chemical Engineering, Nanjing University, Nanjing 210023, P. R. China;* orcid.org/0000-0002-6741-5302; Phone: +86 25 89683593; Email: hxju@nju.edu.cn; Fax: +86 25 89683593

Qin Wei − *Key Laboratory of Interfacial Reaction & Sensing Analysis in Universities of Shandong, Collaborative Innovation Center for Green Chemical Manufacturing and Accurate Detection, School of Chemistry and Chemical Engineering, University of Jinan, Jinan 250022, P. R. China; Department of Chemistry, Sungkyunkwan University, Suwon 16419, Republic of Korea;* orcid.org/0000-0002-3034-8046; Phone: +86 53182765730; Email: sdjndxwq@163.com; Fax: +86 53182765730

Authors

Xue Dong − *Key Laboratory of Interfacial Reaction & Sensing Analysis in Universities of Shandong, Collaborative Innovation Center for Green Chemical Manufacturing and Accurate Detection, School of Chemistry and Chemical Engineering, University of Jinan, Jinan 250022, P. R. China*

Qingze Zeng − *Key Laboratory of Interfacial Reaction & Sensing Analysis in Universities of Shandong, Collaborative Innovation Center for Green Chemical Manufacturing and Accurate Detection, School of Chemistry and Chemical Engineering, University of Jinan, Jinan 250022, P. R. China*

Li Dai − *Key Laboratory of Interfacial Reaction & Sensing Analysis in Universities of Shandong, Collaborative Innovation Center for Green Chemical Manufacturing and Accurate Detection, School of Chemistry and Chemical Engineering, University of Jinan, Jinan 250022, P. R. China*

Xiang Ren − *Key Laboratory of Interfacial Reaction & Sensing Analysis in Universities of Shandong, Collaborative Innovation Center for Green Chemical Manufacturing and Accurate Detection, School of Chemistry and Chemical Engineering, University of Jinan, Jinan 250022, P. R. China;* orcid.org/0000-0002-4321-4282

Wei Cao − *Key Laboratory of Interfacial Reaction & Sensing Analysis in Universities of Shandong, Collaborative Innovation Center for Green Chemical Manufacturing and Accurate Detection, School of Chemistry and Chemical Engineering, University of Jinan, Jinan 250022, P. R. China;* orcid.org/0000-0003-0301-1189

Complete contact information is available at: https://pubs.acs.org/10.1021/acs.analchem.3c02861

Notes

The authors declare no competing financial interest.

ACKNOWLEDGMENTS

This study was supported by the National Natural Science Foundation of China (nos. 22206056 and 22274062), the Shandong Provincial Natural Science Foundation (nos. ZR2022QB117 and ZR2022MB089), and the Jinan Scientific Research Leader Workshop Project (no. 2019GXRC027). The authors thank Yankai Li and Yingchun Li from Shiyanjia Lab (www.shiyanjia.com) for XPS analysis.

REFERENCES

(1) Solano, M. E.; Arck, P. C. *Front. Immunol.* **2020**, 10.
(2) Suo, D.; Fan, X.; Xiao, Z.; Wei, S.; Wang, S.; Wang, P. *Food Chem.* **2021**, *361*, No. 130115.
(3) Kroupova, H. K.; Grimaldi, M.; Sauer, P.; Borik, A.; Zalohova, K.; Balaguer, P. *Sci. Total Environ.* **2023**, *859*, No. 160232.
(4) Diamanti-Kandarakis, E.; Bourguignon, J.-P.; Giudice, L. C.; Hauser, R.; Prins, G. S.; Soto, A. M.; Zoeller, R. T.; Gore, A. C. *Endocr. rev.* **2009**, *30*, 293−342.
(5) Jimenez, G. C.; Eissa, S.; Ng, A.; Alhadrami, H.; Zourob, M.; Siaj, M. *Anal. Chem.* **2015**, *87*, 1075−1082.
(6) Yuhan, J.; Zhu, L.; Zhu, L.; Huang, K.; He, X.; Xu, W. *J. Controlled Release* **2022**, *346*, 405−420.
(7) Qi, S.; Duan, N.; Khan, I. M.; Dong, X.; Zhang, Y.; Wu, S.; Wang, Z. *Biotechnol. Adv.* **2022**, *55*, No. 107902.
(8) Li, L.; Xu, S.; Yan, H.; Li, X.; Yazd, H. S.; Li, X.; Huang, T.; Cui, C.; Jiang, J.; Tan, W. *Angew. Chem. Int. Edit.* **2021**, *60*, 2221−2231.

(9) Sanchez-Bascones, E.; Parra, F.; Lobo-Casta, M. J. *TrAC, Trends Anal. Chem.* **2021**, *143*, No. 116349.
(10) Chen, W.; Zhao, X.; Yang, N.; Li, X. *Angew. Chem.* **2022**, *62*, No. e202209813.
(11) Wang, Y.; Liu, X.; Wu, L.; Ding, L.; Effah, C. Y.; Wu, Y.; Xiong, Y.; He, L. *Biosens. Bioelectron.* **2022**, *195*, No. 113661.
(12) Zheng, Y.; Zhang, L.; Zhao, J.; Li, L.; Wang, M.; Gao, P.; Wang, Q.; Zhang, X.; Wang, W. *Theranostics* **2022**, *12*, 2095−2114.
(13) Stephens, M. *Pharmacol. Ther.* **2022**, *238*, No. 108173.
(14) Tang, X.; Feng, C.; Pan, Q.; Sun, F.; Zhu, X. *TrAC, Trends Anal. Chem.* **2021**, *145*, No. 116456.
(15) Zhu, S.; Han, S.; Zhang, L.; Parveen, S.; Xu, G. *Nanoscale* **2011**, *3*, 4589−4592.
(16) Li, Y.; Gao, X.; Fang, Y.; Cui, B.; Shen, Y. *Coord. Chem. Rev.* **2023**, *485*, No. 215136.
(17) Sun, D.; Lu, J.; Zhang, L.; Chen, Z. *Anal. Chim. Acta* **2019**, *1082*, 1−17.
(18) Tian, D.; Wang, J.; Zhuang, Q.; Wu, S.; Yu, Y.; Ding, K. *Food Chem.* **2023**, *404*, No. 134183.
(19) Wang, Q.; Yang, Q.; Wu, W. *Crit. Rev. Food Sci. Nutr.* **2022**, *62*, 2495−2507.
(20) Wen, J.; Jiang, D.; Shan, X.; Wang, W.; Xu, F.; Shiigi, H.; Chen, Z. *Microchem. J.* **2022**, *172*, No. 106927.
(21) Liu, X.; Li, L.; Luo, L.; Bi, X.; Yan, H.; Li, X.; You, T. *J. Colloid Interface Sci.* **2021**, *586*, 103−109.
(22) Shi, J.; Zhu, M.; Du, W.; Liu, T.; Zhou, L.; Jiang, Y.; Shao, J. *Appl. Surf. Sci.* **2022**, *579*, No. 152192.
(23) Liu, S.; Hu, X. P.; Liu, Q.; Guo, J. W.; Wu, J. Y.; Zhu, W. *Corros. Sci.* **2022**, *208*, No. 110712.
(24) Zeng, X.; Tong, X.; Liu, Z.; Xiong, Y.; Cao, Q.; Cheng, X. *J. Eur. Ceram. Soc.* **2022**, *42*, 3542−3549.
(25) Irfan, M.; Li, A.; Zhang, L.; Ji, G.; Gao, Y. *Fuel* **2021**, *286*, No. 119408.
(26) Li, R.; Wu, L.; Chang, G.; Ke, S.; Wang, Y.; Yao, Y.; Zhang, Y.; Li, J.; Yang, X.; Chen, B. *ACS Appl. Mater. Interfaces* **2022**, *14*, 5887−5896.
(27) Huai, X.; Girardi, L.; Lu, R.; Gao, S.; Zhao, Y.; Ling, Y.; Rizzi, G. A.; Granozzi, G.; Zhang, Z. *Nano Energy* **2019**, *65*, No. 104020.
(28) Li, G.; Jang, H.; Liu, S.; Li, Z.; Kim, M. G.; Qin, Q.; Liu, X.; Cho, J. *Nat. Commun.* **2022**, *13*, 1270.
(29) Liu, D.; Yang, G.; Zhang, X.; Chen, S.; Yuan, R. *Sens. Actuators, B* **2021**, *329*, No. 129210.
(30) Hong, G.; Su, C.; Lai, M.; Huang, Z.; Weng, Z.; Chen, Y.; Deng, H.; Chen, W.; Peng, H. *Anal. Chem.* **2022**, *94*, 12500−12506.
(31) Yuan, F.; Hao, K.; Sheng, S.; Fereja, T. H.; Ma, X.; Liu, F.; Zafar, M. N.; Lou, B.; Tian, H.; Xu, G. *Electrochim. Acta* **2020**, *329*, No. 135117.
(32) Duan, X.; Zhang, N.; Li, Z.; Zhang, L.; Sun, F.; Zhou, Z.; Liu, H.; Guo, Y.; Sun, X.; Jiang, J.; Zhang, D. *J. Colloid Interface Sci.* **2023**, *632*, 171−178.
(33) Guo, L.; Mu, Z.; Qing, M.; Zhou, J.; Li, H.; Wang, L.; Zhong, M.; Bai, L. *Adv. Healthcare Mater.* **2022**, *12*, No. 2202287.
(34) Song, X.; Zhao, L.; Zhang, N.; Liu, L.; Ren, X.; Ma, H.; Kuang, X.; Li, Y.; Luo, C.; Wei, Q. *Anal. Chem.* **2023**, *95*, 1582−1588.
(35) Liu, X.; Bai, L.; Cao, X.; Wu, F.; Yin, T.; Lu, W. *Anal. Chim. Acta* **2022**, *1234*, No. 340522.
(36) Huang, W.; Hu, G.-B.; Yao, L.-Y.; Yang, Y.; Liang, W.-B.; Yuan, R.; Xiao, D.-R. *Anal. Chem.* **2020**, *92*, 3380−3387.
(37) Fu, Y.; Yu, Q.; Zhang, Q.; Zhang, X.; Du, C.; Chen, J. *Biosens. Bioelectron.* **2021**, *192*, No. 113547.
(38) Sun, Y.; Hu, Z.; Zhao, D.; Zeng, K. J. A. A. M. *ACS Appl. Mater. Interfaces* **2017**, *9*, 32202−32210.
(39) Ul Haq, I.; Li, S. H.; Zhen, H.-G.; Khan, R.; Zhang, A.-S.; Zhao, Z.-P. *Chem. Eng. J.* **2020**, *402*, No. 125980.
(40) Luo, Y.; Yang, Y.; Wang, L.; Wang, L.; Chen, S. *J. Alloys Compd.* **2022**, *906*, No. 164369.
(41) Ouyang, X.; Wu, Y.; Guo, L.; Li, L.; Zhou, M.; Li, X.; Liu, T.; Ding, Y.; Bu, H.; Xie, G.; Shen, J.; Fan, C.; Wang, L. *Angew. Chem. Int. Edit.* **2023**, DOI: 10.1002/anie.202300893.
(42) Wang, M.; Liu, J.; Liang, X.; Gao, R.; Zhou, Y.; Nie, X.; Shao, Y.; Guan, Y.; Fu, L.; Zhang, J.; Shao, Y. *Anal. Chem.* **2021**, *93*, 4528−4535.
(43) Dong, X.; Zhao, G.; Li, Y.; Zeng, Q.; Ma, H.; Wu, D.; Ren, X.; Wei, Q.; Ju, H. *Anal. Chem.* **2022**, *94*, 12742−12749.
(44) Wang, Y.; Zhao, G.; Chi, H.; Yang, S.; Niu, Q.; Wu, D.; Cao, W.; Li, T.; Ma, H.; Wei, Q. *J. Am. Chem. Soc.* **2021**, *143*, 504−512.
(45) Dong, X.; Zhang, X.; Du, Y.; Liu, J.; Zeng, Q.; Cao, W.; Wei, Q.; Ju, H. *Biosens. Bioelectron.* **2023**, *236*, No. 115437.
(46) Du, Y.; Zhang, X.; Jia, Y.; Feng, R.; Wu, T.; Zhang, N.; Ju, H. *Anal. Chem.* **2022**, *95*, 1461−1469.
(47) Yang, L.; Wu, T.; Du, Y.; Zhang, N.; Feng, R.; Ma, H.; Wei, Q. *Anal. Chem.* **2021**, *93*, 16906−16914.